Geochemistry, Geophysics, Geosystems®

RESEARCH ARTICLE
10.1029/2021GC010082

Faulting and Magmatic Accretion Across the Overlapping Spreading Center Between Vance Segment and Axial South Rift, Juan de Fuca Ridge

M. Le Saout[1,2], D. A. Clague[1], and J. B. Paduan[1]

[1]Monterey Bay Aquarium Research Institute, Moss Landing, CA, USA, [2]Now at Department of Magmatic and Hydrothermal Systems, GEOMAR Helmholtz Centre for Ocean Research, Kiel, Germany

Key Points:

- Autonomous underwater vehicle mapping of an overlapping spreading center reveals the proportion of faulting and eruptions that occurred during the last ~1300–1450 years
- Faulting at the Vance Segment accommodates ~3/4 of the spreading and magmatic accretion along Axial Seamount south rift accounts for ~1/4
- The spreading axis is <250 m wide along the Vance Segment but ~4 km wide along the south rift of Axial Seamount

Correspondence to:
M. Le Saout,
mlesaout@geomar.de

Citation:
Le Saout, M., Clague, D. A., & Paduan, J. B. (2022). Faulting and magmatic accretion across the overlapping spreading center between Vance Segment and Axial south rift, Juan de Fuca Ridge. *Geochemistry, Geophysics, Geosystems*, *23*, e2021GC010082. https://doi.org/10.1029/2021GC010082

Received 5 AUG 2021
Accepted 17 DEC 2021

Abstract Plate divergence along mid-ocean ridges is accommodated through faulting and magmatic accretion, and, at overlapping spreading centers (OSC), is distributed across two curvilinear overlapping ridge axes. One-meter resolution bathymetry acquired by autonomous underwater vehicles, combined with distribution and ages of lava flows, is used to: (a) analyze the spatial and temporal distribution of flows, faults, and fissures in the OSC between the distal south rift zone of Axial Seamount and the Vance Segment, (b) locate spreading axes, (c) calculate extension, and (d) determine the proportion of extension accommodated at the surface by faults and fissures versus volcanic extrusion over a period of ~1300–1450 years. Our study reveals that in the recent history of the ridges, extension over a distance of 14 km across the Axial/Vance OSC was asymmetric in proportion and style: faults and fissures across 1–2 km of the Vance axial valley accommodated ~3/4 of the spreading, whereas dike-fed eruptions contributed ~1/4 of the extension and occurred across 4 km of the south rift of Axial Seamount.

Plain Language Summary Along mid-ocean ridges, oceanic plates separate through the formation and growth of faults and the emplacement of dikes supplying lava flows. Where segments overlap in a zone of separation, these processes are distributed along two spreading axes separated by 2–30 km kilometers. We combine 1-m resolution bathymetry collected by autonomous underwater vehicles and the age of large lava flows to (a) analyze the distribution of faults and lava flows where Axial Seamount overlaps with the Vance Segment, (b) define the current plate boundary, (c) calculate the speed of plate separation, and (d) determine the proportion and locations of fault extension versus flow emplacement. Our study shows that during the last ~1300–1450 years, fault formation and growth along the Vance Segment are the main contributor to plate separation. In contrast, the emplacement of dikes and lava flows along Axial Seamount account only for ~1/4 of the plate separation.

1. Introduction

Plate divergence along mid-oceans ridges is accommodated through faulting and magmatic accretion (e.g., Bohnenstiehl & Carbotte, 2001; Cowie et al., 1993; Escartín et al., 2007). Studies have shown that the long-term proportion of tectonic versus magmatic extension is highly variable and sensitive to spreading rate (Buck et al., 1998), with the ratio of magmatic accretion over faulting higher along fast-spreading ridges (Buck et al., 2005; Cowie et al., 1993; Escartín et al., 2007; Ito & Behn, 2008; Olive & Dublanchet, 2020). Analysis of fault dimensions and distribution indicate that the proportion of the extension accommodated by magmatism (referred to as *M*) exceeds ~0.9 along fast-spreading ridges (Buck et al., 2005; Cowie et al., 1993; Escartín et al., 2007), is between ~0.7 and 0.95 for intermediate-spreading ridges (Ito & Behn, 2008) and is between ~0.2 and ~0.8 for slow-spreading ridges (Behn & Ito, 2008; MacLeod et al., 2009; Olive & Escartín, 2016; Schouten et al., 2010). More specifically, magma supply controls the ratio between magmatic and tectonic extension, with an increase in magma supply associated with an increase in the proportion of magmatic accretion, resulting in significant variability in *M* (Behn & Ito, 2008; Neumann & Forsyth, 1993; Phipps Morgan & Chen, 1993; Shaw & Lin, 1996; Sleep, 1975). This relationship contributes to variations in axial morphology at similar spreading rates (Canales et al., 2005; Detrick et al., 2002; Le Saout et al., 2019; Sinton et al., 2002). Several detailed studies have analyzed the proportion of the extension accommodated by tectonic features (e.g., Deschamps et al., 2007; Escartín et al., 1999, 2007; Le Saout et al., 2018), but such analyses remain subject to uncertainties. Indeed, the proportion of faults and fissures is often underestimated as it is affected by data resolution and the frequent resurfacing of the seafloor by successive

eruptions. Escartín et al. (2007) estimated that up to 80% of faults and fissures are buried under young lava flows at the 9°N segment of the EPR. In addition, faulting does not exclusively result from amagmatic extension but can also develop out of the accomodation of the stress caused by dike intrusion (e.g., Chadwick & Embley, 1998; Head et al., 1996; Rubin, 1992), magmatic inflation, plate bending, as well as cooling (Escartín et al., 2007; Shah & Buck, 2003).

Overlapping spreading centers (OSC) are common non-transform offsets along fast- and intermediate-spreading rate ridges (e.g., Carbotte et al., 2015; Macdonald et al., 1988; Schouten et al., 1985). They mark regions where accretionary processes occur along two curvilinear overlapping ridges axes, offset by 2–30 km (Macdonald & Fox, 1983; Macdonald et al., 1992) over a distance of 10–50 km. Due to segment scale variations in tectonic and volcanic features, OSC are commonly proposed to occur above regions of lower magma supply (Macdonald et al., 1988, 1992; Schouten et al., 1985). However, seismic reflection studies have imaged large melt volumes beneath some OSC (Kent et al., 2000; VanderBeek et al., 2016), and White et al. (2009) proposed that the apparent lower magma supply at OSCs results from diffuse volcanism and crustal deformation, where the plate divergence accommodated by tectonic and magmatic activity is distributed over tens of kilometers. On the Juan de Fuca ridge, the northern end of the Vance Segment and the South Rift Zone (SRZ) of Axial Seamount, called here Vance/Axial OSC, overlap in a broad deformed zone. On the west side, the SRZ axial high morphology reflects high magma supply resulting from the interaction between the ridge and Cobb hotspot (Chadwick et al., 2005). On the east, the Vance Segment's axial valley indicates lower magma supply. As the magma supply varies, the extension style and thus the proportion of faults should also be affected (Behn & Ito, 2008). Whereas examination of deformation over large distances and time is often complicated by the variation in flow ages, the Vance/Axial OSC is partially flooded by a single voluminous SRZ flow (Appelgate, 1990; Paduan et al., 2020). This voluminous flow is the earliest of five that erupted ∼1307 calibrated radiocarbon yr BP (Before Present) (Clague et al., 2019), where present is 1950 CE. Across the OSC these five extensive flows of similar age and composition record extension during the ∼1300–1450 years before the AUV mapping data were collected in 2016. The inferred constant age of the flows on both limbs of the Vance/Axial OSC provide a rare opportunity to analyze fault distribution and measure extension.

In this study, bathymetry of the Vance/Axial OSC collected by autonomous underwater vehicles (AUVs) provided the basemap for measuring the offsets of faults and defining the extent of individual flows. The detailed analysis permits assessment of extension across the OSC by: (a) identifying the spreading axes on the Vance Segment and the SRZ, (b) calculating the horizontal displacement accommodated by faulting, and (c) determining the distribution of the extension across the OSC during the last ∼1300–1450 years.

2. Geological Setting

The Vance Segment and the Axial Segment that includes Axial Seamount and its north and south rift zones are two of the seven segments of the Juan de Fuca ridge. Their spreading rates are constrained by magnetic isochrons that provide an average rate over the last 0.78 Ma. Wilson (1993) estimated a spreading rate of 52 and 53 mm/yr for the Vance and Axial segments, respectively. The revised MORVEL (for mid-ocean ridge velocity) model of DeMets et al. (2010), yields slightly slower spreading rates of 49.5 and 50 mm/yr for the Vance and Axial Segments, respectively. Between 45°28.2′N and 45°40.2′N, the two axes are offset by ∼6.5 km and overlap for ∼30 km (Figure 1). North of the OSC, Axial Seamount is the youngest seamount of the Cobb-Eickelberg seamount chain and results from the interaction of the Juan de Fuca ridge and Cobb hotspot (Chadwick et al., 2005). From its summit caldera, rift zones extend 50 km to the north and south (Chadwick et al., 2005). The rifts are fed by dikes propagating laterally from a central magma reservoir below the Axial Seamount caldera (Caress et al., 2012; Chadwick et al., 2016; Dziak & Fox, 1999). Both rifts are broad axial highs dominated by volcanic accretion (Appelgate, 1990; Chadwick et al., 2005). Of the three historical eruptions (in 1998, 2011, and 2015), only the one in 2011 produced a pillow ridge within the OSC, emplaced at the north edge (Figure 1; Caress et al., 2012; Clague et al., 2017). The dike of the 1998 eruption was seismically detected to have propagated farther into the OSC (Dziak & Fox, 1999) but there is no evidence of flows emplaced south of the upper rift zone (Chadwick et al., 2013); the 2015 eruption propagated north (Chadwick et al., 2016).

South of Axial Seamount, the Vance Segment is 70 km long and ∼6–7 km wide, and the 200–250 m deep axial valley encloses a segmented low-relief axial volcanic ridge (AVR) that is <100 m high (Canales et al., 2005;

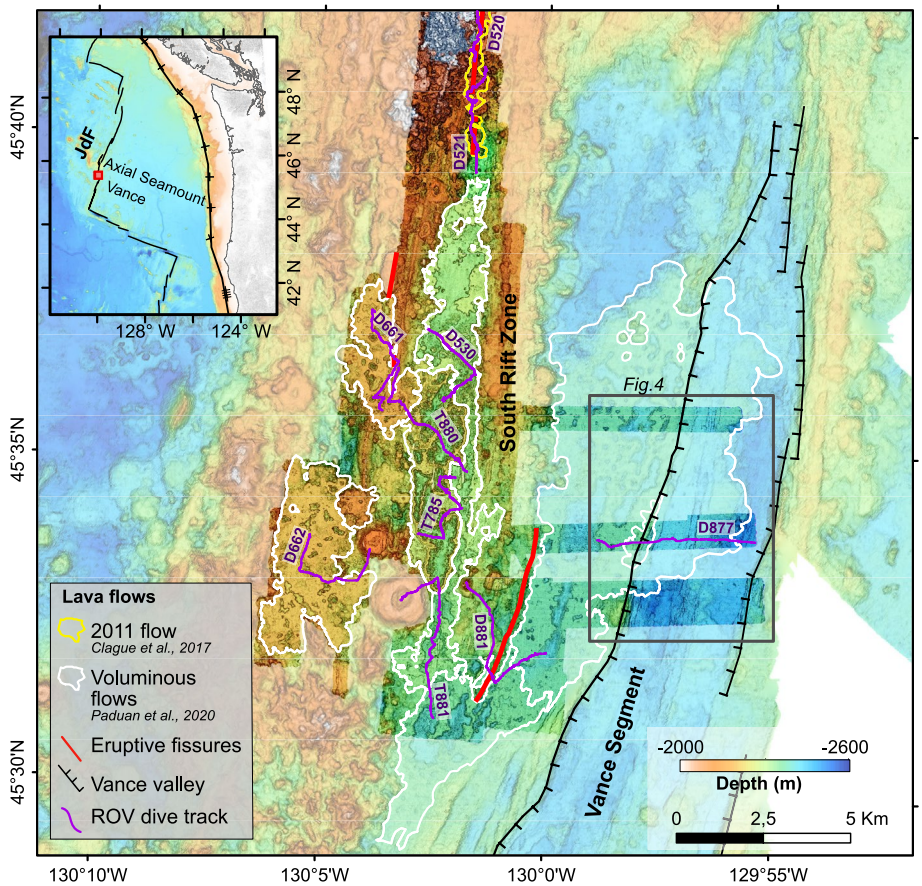

Figure 1. Overview map of the overlapping spreading center (OCS) between the South Axial Rift Zone (SRZ) and the Vance Segment. The 1 m resolution AUV bathymetry is superposed on faded, lower-resolution ship-based bathymetry. The voluminous flows (Paduan et al., 2020) and the hummocky ridge from the 2011 eruption (Clague et al., 2017) are outlined in white and yellow, respectively. Recent eruptive fissures along the SRZ are red lines, and the thin black lines delineate the walls of the axial valley of the Vance Segment. ROV dive tracks are in purple with the dive number indicated. The gray box locates the extent of Figure 3. The inset shows the OSC location (red dot) along the Juan de Fuca Ridge offshore of the Pacific Northwest coast.

Carbotte et al., 2006). North of 45°20′N, Appelgate (1990) locates the AVR on the eastern side of the valley. Seismic reflection profiles reveal a discontinuous 0.6–1.7 km wide magma lens 2.5 km below the seafloor (Canales et al., 2005; Carbotte et al., 2006). This shallow magma lens does not extend north of 45°30′N, however a deeper (~6 km deep) subcrustal magma body is interpreted to extend slightly west of the axial valley under the OSC between 45°34′N and 45°38′N (Lee & Carbotte, 2019). No eruptions have been recorded in recent years along the entire Vance Segment.

Sea MARC I side-scan sonar data collected in 1986 (Appelgate, 1990) show an extensive lava flow within the northern Vance Segment. The high backscatter indicates that it is more recent than the surrounding flows. The flow can be traced from the SRZ eastward into the axial valley of the northern Vance Segment (Appelgate, 1990). The source of this flow on the Axial SRZ has been confirmed with AUV mapping and ROV sampling (Clague et al., 2019; Paduan et al., 2020). This lava flow is estimated to be on the order of 40 m thick for a volume of 2.1 km^3. It is the oldest of five voluminous flows emplaced ~1300–1450 years ago (Figure 2). The five flows are proposed to have evacuated the crustal magma reservoir, thereby triggering the formation of the Axial Seamount caldera (Clague et al., 2019).

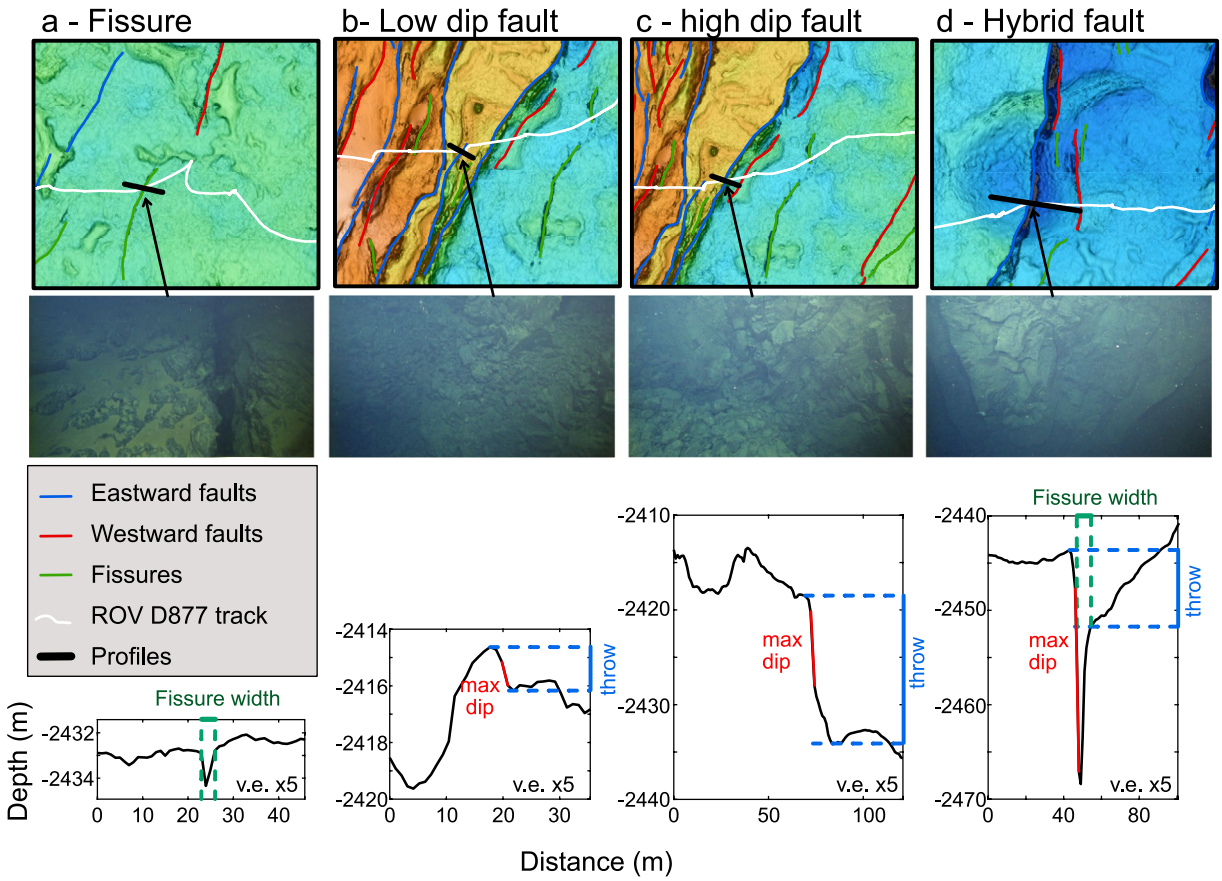

Figure 2. Illustration of the different fracture type (a) Fissure, (b and c) Faults, and (d) Hybrid faults in map and profile view. The photos from ROV dive D877 show (a) fissure, (b) talus block at the foot of a fault scarp, and (c and d) sub-vertical fault scarps. The method of measurement of throw (fault height in blue), maximum dip (red) and fissure width (in green) is indicated on the bathymetric profiles. Vertical exaggeration (v.e.) x5.

3. Data and Method

3.1. Data

The analysis presented is based primarily on the geological interpretation of AUV bathymetric mapping, supported by visual observations and sampling. From 2009 to 2019, the SRZ and part of the Vance Segment were surveyed with the MBARI mapping AUVs, covering roughly 108 km^2 of the OSC, including 9 km^2 of the axial valley of the Vance Segment. The AUVs were equipped with Reson 7125 400 kHz multibeam sonars, and flown 50 m above the seafloor. The survey lines are spaced ∼150 m to produce sufficient overlap. The AUVs are equipped with Kearfott SeaDevil inertial navigation systems (INS) including a Doppler velocity log (DVL), accelerometers, and a ring laser gyro. The navigation deviation is estimated at 0.05% of the distance traveled (Caress et al., 2008) Bathymetric data were process using MB-system (Caress & Chayes, 2011) that allows automated and manual editing of the navigation and bathymetry. The resulting computed grid has ∼1 m lateral resolution and ∼10 cm vertical resolution (Figure 1). In addition to AUV mapping, the MBARI remotely operated vehicles (ROV) *Tiburon* and *Doc Ricketts* provided targeted geological sampling and observations. Seven ROV dives on the deep SRZ of Axial, two along the 2011 lava flow and one across the Vance Segment (Figure 1) collected seafloor video, rock samples, and sediment cores for radiocarbon dating.

3.2. Terminology

Axial valley, as used here, refers to the km-scale morphology of the Vance Segment whereas graben refers to the smaller trough formed within the axial valley in the recent history of the Vance Segment. Fracture is used as a generic term englobing the three types of tectonic features observed. Fissure refers to an extensional fracture

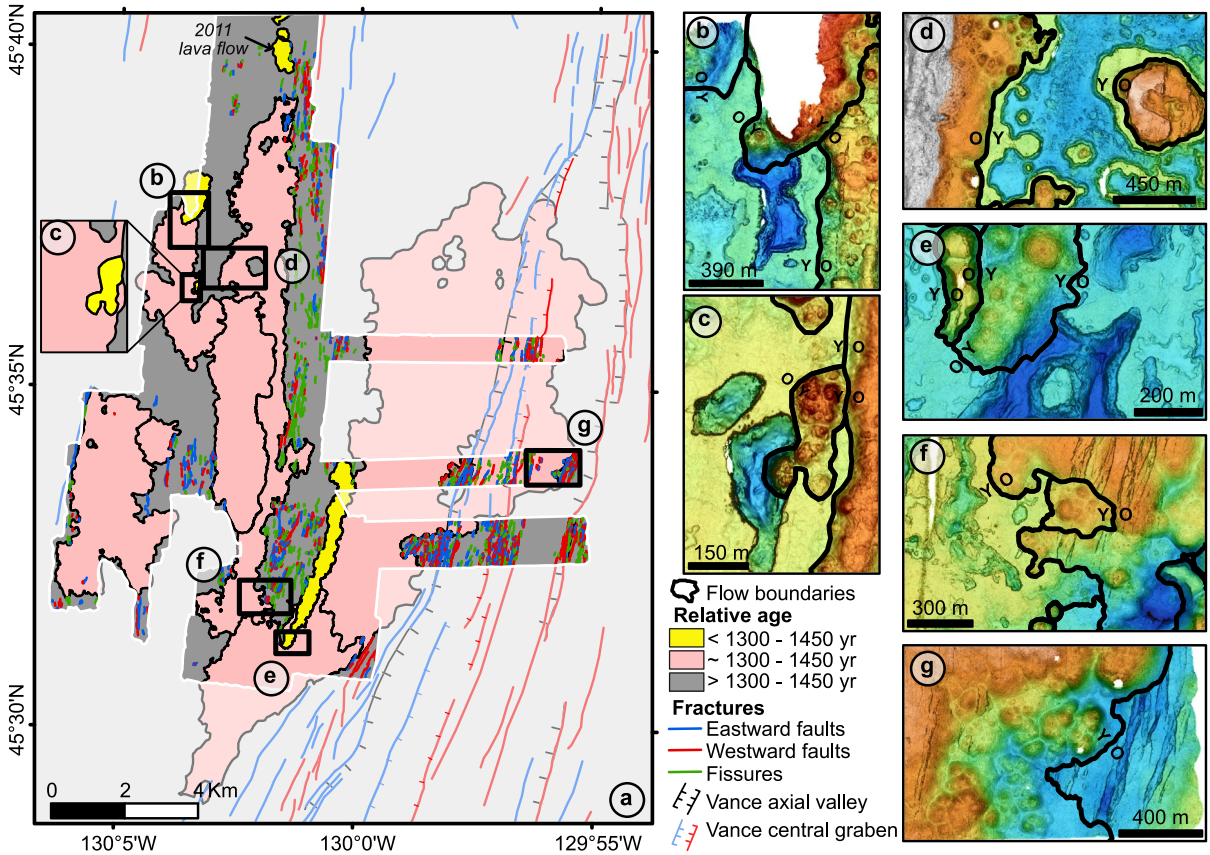

Figure 3. (a) Geological interpretation of the AUV-bathymetric map of the Vance/Axial OCS. The AUV bathymetry is outlined in white. The eastward- and westward-facing faults are indicated by blue and red lines, respectively, and fissures are in green. The axial valley and central graben of the Vance Segment are delineated. When possible, the faults were extended based on the ship-based bathymetry. The flow ages indicated are relative to the emplacement of the voluminous flows (in light pink). The younger flows are shown in yellow, and the older lava flows in gray. (b–g) The black boxes locate the six close-ups, showing the relationship between lava flows and fractures used to determine relative ages. Y (young) and O (old) letters on the lava flow outline indicate the relationship at the contact.

(Figure 2a) that consists of two nearby facing scarps of similar height and length forming a V-shape cross-section (Figure 2a). Fault refers to a fracture displaying a shear motion perpendicular to its surface resulting in a vertical displacement (Figures 2b and 2c). Finally, hybrid faults display both extensional and shear movement resulting in an extensional fissure at the bottom of a scarp (Figure 2d). Hybrid faults represent the transition from fissures to faults (e.g., Deschamps et al., 2007; Ramsey & Chester, 2004).

3.3. Methods

Relative ages are determined based on the stratigraphic relationships between lava flows, patterns of fracture distribution and sediment cover, and geometry at the flow front. For the latter, examination of the AUV data shows that collapses in younger flows tend to contour the flow fronts of older lava flows (Figure 3d), and older collapses can be partially or totally filled by younger lava flows (Figures 3b, 3c, and 3e). Similarly, fractures can be partially or completely erased by younger lava flows (Figures 3f and 3g).

Faults and fissures are manually digitized based on the bathymetry and derive slope map. Fissures are digitized following their centerlines, and faults (including hybrid faults) are digitized following the fault crest. Fault throw (height), dip and fissure width are measured along five 1-m-resolution bathymetric profiles, perpendicular to the ridge axis of the Vance Segment and spaced roughly 250 m apart (Figure 4). Only tectonic features younger than the voluminous flow are taken into account. Erosion, mass wasting and data resolution are parameters that generally affect the apparent fault geometry (Escartín et al., 1999; Howell et al., 2016; Le Saout et al., 2018, 2019). Faults and fissures with horizontal and vertical components less than 1.8 and 0.5 m, respectively, are not apparent

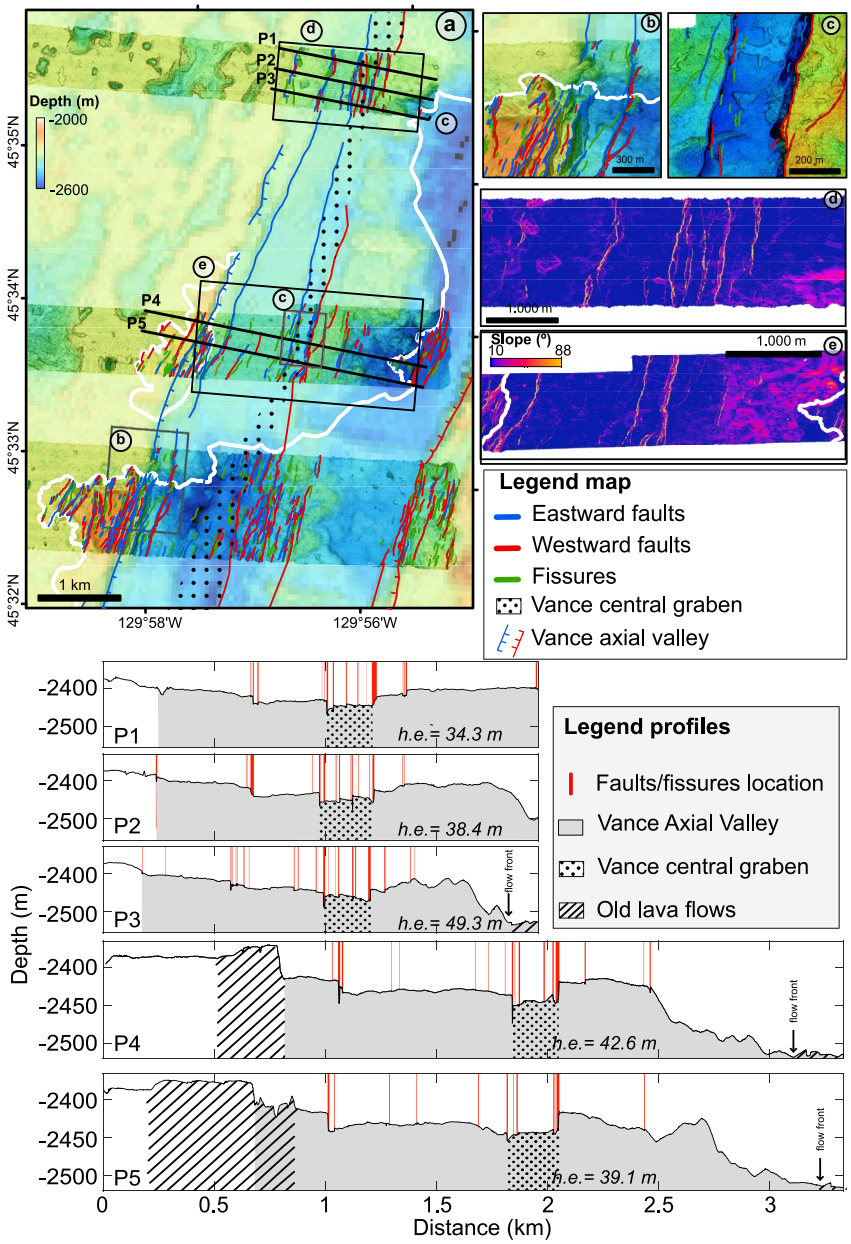

Figure 4. (a) Bathymetric map of the axial valley of the Vance Segment. The 1-m resolution AUV data overlays 30 m resolution ship-collected Simrad EM302 bathymetry (Chadwick, 2013). The eastward- and westward-facing faults are indicated in blue and red, respectively, and fissures are shown in green. The white line shows the eastern margin of the voluminous lava flow. The gray boxes are close-ups showing (b) the burial of the western wall of the axial valley by the voluminous flow in the northern half of the image and (c) the continuity of the lava flow structures (i.e., lava ponds, inflations) across the graben formed since the flow erupted. (d and e) Slope map across the axial valley of the Vance Segment highlighting fault and fissure escarpments. The five bold black lines locate the bathymetric profiles (P1 to P5) used to determine horizontal displacement perpendicular to the Vance axis. On the bathymetric profiles, the extent of the Vance axial valley is indicated by the gray background and the location of flows older than the voluminous ~1300–1450 year-old flow by the striped pattern. The central graben is indicated by the dot pattern on the bathymetric profiles and map (a). The vertical red lines locate fissures and faults, and their thicknesses illustrate the different horizontal displacements associated with each feature. The cumulative horizontal extension (h.e.) is indicated for each profile.

in the bathymetry. To avoid underestimations due to erosion and mass wasting, the throw is measured from the shallowest part of the fault down to the deepest part (Figures 2b and 2c, Escartín et al., 1999; Le Saout et al., 2018, 2019), or in the case of hybrid faults, up to the beginning of the fissure (Figure 2d). The measured

dip corresponds to the maximal slope angle measured along the fault scarp. Due to the effect of data resolution on apparent slope dip and heave (horizontal extension), the fault heave is calculated using the scarp height and assuming an original fault dip of 75 ± 5°, as justified in Section 5.2. We estimate that the horizontal and vertical errors derived from the bathymetry are less than 1 and 0.1 m, respectively.

The cumulative extension along each profile is obtained by summing the horizontal displacement associated with each fault and fissure. The extension rate is calculated along the five bathymetric profiles using the cumulative horizontal extension and the underlying flow age. The error on the extension rate associated with the age uncertainties is estimated at 5.5% or about 2 mm/yr.

4. Results

4.1. Lava Flow Relative Ages

In the region of the Axial/Vance OSC, lava flows can be categorized in three groups based on their relationship to the five voluminous flows that all erupted along the SRZ within the timeframe of 1300–1450 years ago (Figure 1, Clague et al., 2019). The first group represents older lava flows emplaced along the Vance Segment and the Axial SRZ prior to the voluminous flows. They are the most densely faulted lava flows. The second group is the five voluminous lava flows (Figure 3a). They cover ∼100 km^2 between 45°28.5′N and 45°41′N. The largest of these flows exceeds 50 km^2 and has a thickness of 30–100 m (Clague et al., 2019; Paduan et al., 2020). It erupted from the SRZ and flowed S and then NE, where it overflowed the west bounding fault of the Vance axial valley and partially filled it. Between 45°28.5′N and 45°41′N, about 25% of the valley floor is covered by this single voluminous flow. The third group consists of four lava flows, including the 2011 distal pillow ridge, that were emplaced on the SRZ since the voluminous lava flows (Figures 3a–3c and 3e). These four 150–700 m wide and up to 5.3 km long hummocky flows are distributed over an area 4.4 km wide (Figure 3).

Where the oldest of the SRZ voluminous flows entered the Vance Segment (closeup shown in Figure 3g), AUV maps and ROV observations showed the Vance lava flow surfaces to be highly fractured and heavily sedimented, and therefore much older.

4.2. Fracture Distribution and Dimension

Faults and fissures are observed all across the OSC. However, the three flow categories have distinct faulting patterns. The older flows (Group 1) are cut by faults and fissures along both the SRZ and the Vance Segment (Figure 3). The young flows (Group 3) present no sign of recent deformation. Finally, the voluminous flows (Group 2) only show deformation in the section located within Vance Segment. Faults and fissures are distributed across an area <1,500 m wide on the west side of Vance Segment. On the west flank, the main faults bounding the Vance axial valley were also erased by the oldest and largest of the voluminous flows, with less than 1 m of horizontal displacement after the emplacement of the lava flow (Figure 4b). Therefore, the detailed tectonic analysis is restricted to the deformation observed in the voluminous flow within the axial valley of the Vance Segment (Figure 4).

Along the five profiles, 17% of the features are purely extensional fissures, 73% are faults, and 10% are hybrid faults and display both extensional and vertical offsets. Fault scarps are up to 37-m high but are usually <10 m high, with dips varying from 6° to 80°. A plot of fault throw versus fault dip (Figure 5a) shows that faults with vertical throw smaller than 5 m have an apparent dip that systematically varies with the fault height, indicating that the measured dip for small scarps is highly affected by the data resolution. This is consistent with ROV dive observations that show that even small scarps are relatively sub-vertical (Figure 2d). Also, talus blocks at the foot of small fault scarp result in a decrease the apparent dip (Figure 2b). Beyond 5 m height, fault dips vary between 49° and 80°, with 56% of dips ranging from 70° to 80° (Figure 5b). Hybrid faults are less than 14 m in height and have up to 7 m wide and 23 m deep fissures at the bottom of the scarp. Fissures distinguished in the bathymetric data are 1–5.5 m wide and 0.3–5.4 m deep. However, the apparent depth is affected by the data resolution and angle of incidence of the sonar beams. Analysis of ROV dive D877 (Figure 1) suggest that 12 of the observed fissure are not apparent on the bathymetry. All these fissures are less than 1 m in width and most are less than 0.5 m. We estimate that they comprise less than 6 m of the extension across the Vance Segment.

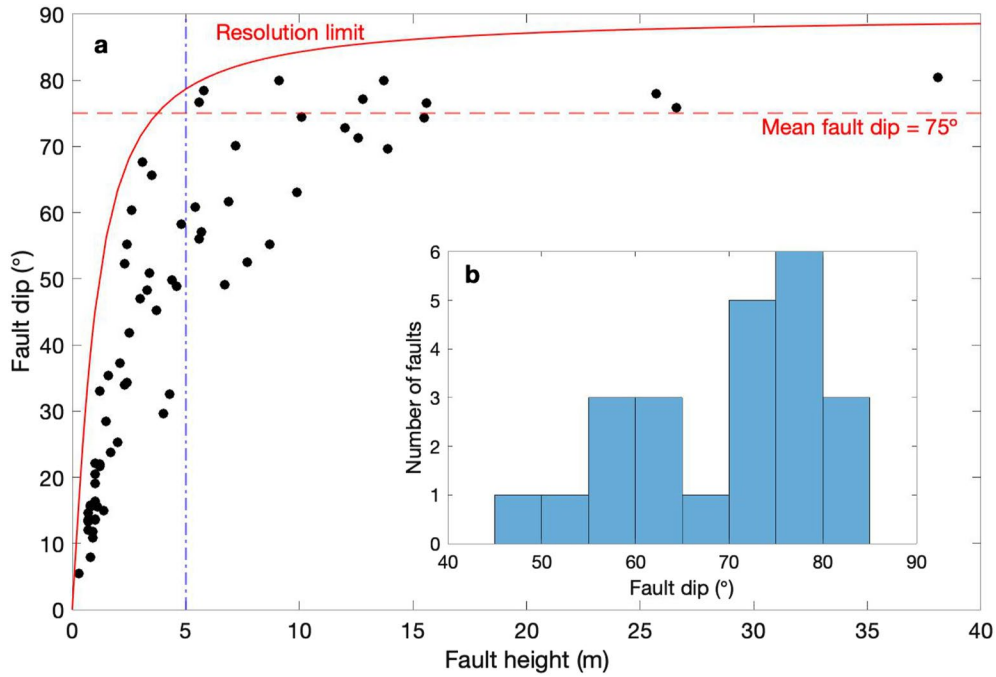

Figure 5. (a) Fault dip versus fault height plot. Apparent dip for smaller fault throw (<5 m high) are affected by the data resolution. The maximum measureable dip based on the data resolution (1 m) is indicated by the red line. The mean fault dip (75°) extracted from dip frequency is indicated by the red dash line. (b) Dip frequency for fault with a throw >5 m.

Due to the effect of data resolution on the measured dip, fault heave is estimated along the five profiles using a dip angle of 75 ± 5° (Figure 5b). Calculated heaves of individual faults vary from <0.1 to 10.2 m ±3.5%. The cumulative heave, and therefore horizontal extension, along the five profiles (Figure 4) ranges from 34.3 to 49.2 m with a mean displacement of 40.7 ± 7.5 m since the emplacement of the voluminous Axial flow. Along the profiles, ~9.3 and 10.3 m of extension was experienced on the western- and eastern-facing faults, respectively. The fissures account for an average of 21.1 m of the extension (12.6 m by purely extensional fissures and 8.5 m by the fissures at the foot of hybrid faults). The deformation is greatest where it has formed a 200–250 m wide central graben within the Vance Segment (Figure 4c). On the west side and east side of the central graben (Figure 4), faults and fissures accommodate in average 19.8 and 20.9 m respectively, meaning that the extension is accommodated relatively symmetrical with respect to the graben center.

5. Discussion

5.1. Extension Across the Vance Segment

The distribution of faults and fissures across the ~1300–1450 year old Axial flow that floods the Vance Segment indicates that the deformation is located within the axial valley and limited to a zone 1–2 km wide with a 200–250 m wide graben in its center. Similarly the western valley wall has been efficiently buried with little or no displacement (<1 m) evident over the same period. The absence of significant vertical and horizontal movement along the valley wall is consistent with the model from Carbotte et al. (2006), which hypothesized that the faults bounding the axial valley on each side of Vance AVR are inactive and that the extension is accommodated in the segment center. Based on this model, it is assumed that little to no extension was accommodated on the eastern valley wall during the same period. We also observed that while faults and fissures are numerous in the older seafloor east of the voluminous flow, they are completely buried at the flow contact and show no sign of reactivation. Thus, the total extension accommodated by faults and fissures across the Vance axial valley is 40.7 ± 7.5 m since the emplacement of the voluminous axial flow. The relatively large variations in the horizontal displacement and associated extension rate from the profiles could reflect short-length variation in extension, or most probably, changes in how the extension is accommodated. Either reactivation of pre-existing faults or formation of new

fissures or faults smaller than the resolution thresholdwould not be accounted for. Observations along the ROV dive D877 suggest that ∼15% of the extension could be under the resolution threshold.

The deformation occurs over 1–2 km across the Vance Segment but is concentrated in a 200–250 m wide graben within the valley (Figure 3c). The symmetry of the extension on both sides of the graben axis indicates that during the recent history of the Vance Segment, the spreading axis is located at the graben center, offset toward the west by ∼600 m relative to the axial valley center. The graben is observed in the ship-based bathymetry, which shows that it extends from 45°03′N to 45°41′N. This assessment is contrary to previous studies that located the spreading axis on the east side of the valley (Appelgate, 1990; Canales et al., 2005) based on the presence of a topographic high that is inferred to be an axial volcanic ridge. The apparent topographic high could, however result from subsidence of the west side of the valley or reveal a jump of the spreading axis toward the west similar to that observed along Alarcon Rise in the Gulf of California (Le Saout et al., 2019).

5.2. Origin of the Faults and Fissures Across Vance Segment

Extension across the Vance Segment, as along all ridge segments, could be caused by the tectonic accommodation of plate separation, by the magmatic accommodation of the stress caused by dike intrusion (e.g., Chadwick & Embley, 1998; Head et al., 1996; Pollard et al., 1983; Rubin, 1992), or by some combination of the two. The absence of young lava flows suggests that the faulting observed in the Vance axial valley results primarily from tectonic extension, although we cannot preclude that dike intrusions contribute to the extension. The imaged magma body in the northern section of the Vance Segment is ∼6 km deep below the mapped area (Lee & Carbotte, 2019) making it less likely that dikes originating from such a magma reservoir would reach the surface to produce lava flows. Also, while small offset and fissures (>50% of the extension) are often considered to be very shallow structures that do not penetrate deep in the crust (e.g., Cowie, 1998), the total displacement of those faults and therefore the penetration depth into the crust cannot be estimated. Indeed, the voluminous flow emplaced in an already highly tectonized seafloor efficiently buried previous fault. Therefore the current offset measured could only correspond to the extension along reactivated faults during the last 1300–1450 years.

From previous studies, the horizontal extension associated with dike intrusion is about 2/3 the width of the dike (Mastin & Pollard, 1988). If the extension across the Vance Segment resulted only from successive dike intrusion, 50 to 73 dikes with an average width of 1 m would be necessary to produce the observed 40.7 ± 7.5 m of horizontal extension. Such dikes would have to be emplaced during the ∼1300–1450 years period since the flow that recorded the extension was erupted, requiring one dike every 10–26 years on average. Some dike intrusions could have initiated vertically from the deep magma body, or laterally from farther south on the Vance Segment and propagated several kilometers along axis, as observed during the 2011 Axial Seamount eruption where lava erupted ∼33 km downrift from the origin of the eruption within summit caldera (Clague et al., 2017). No shallow magma lens was imaged within ∼10 km south of the study area (Canales et al., 2005; Carbotte et al., 2006), so repeated lateral dike intrusion is improbable. Some of these hypothetical frequent dike intrusions would have reached the surface to produce volcanic flows. Therefore, most, if not all, the extension measured across the Vance axial graben is tectonic in origin.

5.3. Extension Across the Axial South Rift Zone

The SRZ limb of the OSC is characterized by four hummocky flows that postdate the voluminous flows and an absence of distinguishable faults and fissures over the ∼1300–1450 year period (Figure 2). Some faults and fissures along SRZ could have been buried by those most recent lava flows. However, their relatively small dimension and the absence of distinguishable fractures in the continuity of these flows suggest that if some tectonic deformation occurred prior to their emplacement, it is extremely limited. Thus, the extension along the SRZ is proposed to be only accommodated by dike intrusions that supplied lava to build hummocky pillow ridges. Dike widths along mid-ocean ridges are estimated at 0.5–3 m with an average of 1 m based on measurements in ophiolites (Qin & Buck, 2008) or deduced from graben dimensions (Chadwick & Embley, 1998; Head et al., 1996). As none of the flows overlapped, the contribution to the extension by volcanic accretion along the SRZ could be as minimal as 0.5–3 m if each intrusion is limited to the length of the flow. This is suggested by the absence of fissures extending beyond the hummocky flow and acoustic study of the 2011 eruption also show that the 2011 dike did not propagate further than the 2011 southern flow. However, during the 1998 eruption at Axial Seamount, the

acoustic signal were recorded as far south as 45°27′N (Dziak & Fox, 1999) without evidence of fracture or flow emplacement at the surface. Such observations suggest that a portion of the magmatic extension is not accounted for. Therefore, the total extension could amount to 2–12 m if each dike intrusion (excluding the 2011 eruption and including the 1998 dike intrusion) extends along the entire OSC.

Along the SRZ, the distribution of the younger hummocky flows indicates that extension attributed to dike intrusion occurs over a zone 4.4 km wide, showing that the spreading axis along the distal SRZ is not focused. The broad area of deformation is consistent with previous observations that suggest that OSCs are areas of diffuse volcanism and crustal deformation (White et al., 2009).

5.4. Asymmetry of the Extension and Short-Term Extension Rate

Since ∼1300–1450 years ago, extension across the two limbs of the OSC differs in proportion and style. Based on our calculation, >77% of the extension is accommodated along the Vance Segment and <23% along the SRZ, indicating that the Vance Segment is the main spreading center over this short time period. Across the OSC, <23% of the extension is clearly shown to be accommodated by magmatic intrusion (along the SRZ). This indicate that the OSC is 2–3 times more tectonic-accommodated extension than expected based on the longer timescale average suggested by the ratio of magmatic extension (M) at intermediate-spreading rate ridges which ranges from 0.7 to 0.95 (Ito & Behn, 2008; Olive & Dublanchet, 2020). Such variations likely result from temporal variations in volcanic and tectonic activity and therefore in the underlying plumbing system.

The asymmetry of the extension directly reflect the difference in the ridge system. Indeed the axial-high morphology of the SRZ indicate a long-term higher magmatic input. In addition, the lower proportion of the extension could be directly related with the SRZ plumbing system. The SRZ is fed by dikes propagating laterally from a central magma reservoir below the Axial Seamount Caldera (Caress et al., 2012; Chadwick et al., 2016; Dziak & Fox, 1999), and not all dikes propagate this far, as shown by the 2015 eruption that propagated north of the caldera (Chadwick et al., 2016). In contrast, the Vance Segment is a more typical intermediate ridge system, with a segmented magma lens under the ridge axis (Canales et al., 2005; Carbotte et al., 2006). The axial valley morphology and the absence of a shallow magma lens in the northern section are both consistent with a long-term lower magmatic budget and the, at least short-term, higher tectonic extension observed.

Finally, based on sediment core ages (Clague et al., 2019) we can estimate that over the last ∼1300–1450 years, the total extension rate across the Axial/Vance OSC is ∼29.9 ± 7.1 mm/yr, about 2/3 of the total extension estimated from the spreading rate (DeMets et al., 2010). This difference may result from two factors. First, it could indicate that some of the extension has not been accounted for, due to the underestimation of the deformation caused by data resolution and the limitation of identifying <1 m wide fissures, or an underestimation of the width of deformation and thereby not including deformation occurring further east or west. The difference in the calculated extension rate could also reflect a temporal change in the extension rate as models such as MORVEL (DeMets et al., 2010) estimate long-term extension over the last 0.78 Ma.

6. Conclusion

1. Over a period lasting ∼1300–1450 years, the spreading processes across the Vance/Axial OSC occurred over a width of ∼10 km. The extension measured on faults, fissures and dike-fed eruptions reveals that the accommodation of the plate separation is highly heterogeneous across the OSC.
2. Across the Axial/Vance OSC 3/4 of the extension is accommodated by faults and fissures on the Vance Segment. The absence of shallow magma lens and young eruption suggests that most of the extension across the Vance axial valley is tectonic in origin. In contrast, dike-fed eruptions accommodate less than 1/4 of the extension without evidence of faulting along the SRZ. This asymmetry directly results from differences in the magma budget and plumbing system between the two limbs of the OSC.
3. The fault distribution on the Vance Segment defines a narrow area (<250 m) on the west side of the axial valley that defines the current spreading axis along the northern section of the Vance Segment. In contrast, extension along SRZ is more diffuse and occurs over an area 4.4 km wide.
4. The extension rate estimated for the last ∼1300–1450 years corresponds to 2/3 of the long term extension rate reflecting fluctuation of the extension through time or, perhaps underestimation of the extension.

5. The relative proportions of extension that occurred across the Vance Segment and SRZ indicate that in the recent history of the ridge, the Vance Segment is the principal spreading axis.

Data Availability Statement

The bathymetric data (https://doi.org/10.26022/IEDA/330467), lava flows, faults and fissures outlines (https://doi.org/10.26022/IEDA/330468 and https://doi.org/10.1594/IEDA/324415) are available through the MGDS portal.

Acknowledgments
This study combines over a decade of data collection and would not have been possible without the support of the captains and crews of the R/V *Zephyr* and R/V *Rachel Carson*. The authors thank Dave Caress, Hans Thomas, and the MBARI AUV team for the acquisition of the bathymetric data as well as the pilots of the ROVs *Tiburon* and *Doc Ricketts* for the dives that made flow observations and sampled sediment cores for radiocarbon dating. The authors also thank S. Carbotte, G. Ito, and R. Parnell-Turner for their constructive comments that have helped to improve this manuscript. This project was supported by David and Lucile Packard Foundation through a grant to MBARI. Open access funding enabled and organized by Projekt DEAL.

References

Appelgate, T. B. (1990). Volcanic and structural morphology of the south flank of Axial Volcano, Juan de Fuca Ridge: Results from a Sea MARC I side scan sonar survey. *Journal of Geophysical Research: Solid Earth*, *95*(B8), 12765–12783. https://doi.org/10.1029/jb095ib08p12765

Behn, M. D., & Ito, G. (2008). Magmatic and tectonic extension at mid-ocean ridges: 1. Controls on fault characteristics. *Geochemistry, Geophysics, Geosystems*, *9*, Q08O10. https://doi.org/10.1029/2008GC001965

Bohnenstiehl, D. R., & Carbotte, S. M. (2001). Faulting patterns near 19°30′S on the East Pacific Rise: Fault formation and growth at a superfast spreading center. *Geochemistry, Geophysics, Geosystems*, *2*(9). https://doi.org/10.1029/2001GC000156

Buck, W. R., Delaney, P. T., Karson, J. A., & Lagabrielle, Y. (Eds.). (1998). Faulting and magmatism at mid-ocean ridges. *Geophysical Monograph Series* (Vol. 106). American Geophysical Union. https://doi.org/10.1029/GM106

Buck, W. R., Lavier, L. L., & Poliakov, A. N. B. (2005). Modes of faulting at mid-ocean ridges. *Nature*, *434*(7034), 719–723. https://doi.org/10.1038/nature03358

Canales, J. P., Detrick, R. S., Carbotte, S. M., Kent, G. M., Diebold, J. B., Harding, A., et al. (2005). Upper crustal structure and axial topography at intermediate spreading ridges: Seismic constraints from the southern Juan de Fuca Ridge. *Journal of Geophysical Research: Solid Earth*, *110*(B12). https://doi.org/10.1029/2005jb003630

Carbotte, S. M., Detrick, R. S., Harding, A., Canales, J., Babcock, J., Kent, G., et al. (2006). Rift topography linked to magmatism at the intermediate spreading Juan de Fuca Ridge. *Geology*, *34*, 209. https://doi.org/10.1130/g21969.1

Carbotte, S. M., Smith, D. K., Cannat, M., & Klein, E. M. (2015). Tectonic and magmatic segmentation of the Global Ocean Ridge System: A synthesis of observations. *Geological Society, London, Special Publications*, *420*(1), 249–295. https://doi.org/10.1144/SP420.5

Caress, D. W., & Chayes, D. N. (2011). *MB-System: Open source software for the processing and display of swath mapping sonar data*. Lamont-Doherty Earth Observatory of Columbia University. Retrieved from http://www.mbari.org/products/research-software/mbsystem/

Caress, D. W., Clague, D. A., Paduan, J. B., Martin, J. F., Dreyer, B. M., Chadwick, W. W., et al. (2012). Repeat bathymetric surveys at 1-metre resolution of lava flows erupted at Axial Seamount in April 2011. *Nature Geoscience*, *5*(7), 483–488. https://doi.org/10.1038/ngeo1496

Caress, D. W., Thomas, H., Kirkwood, W. J., McEwen, R., Henthorn, R., Clague, D. A., et al. (2008). High-resolution multibeam, sidescan, and subbottom surveys using the MBARI AUV D. Allan B. In J. R. Reynolds, & H. G. Greene (Eds.), *Marine habitat mapping technology for Alaska* (pp. 47–70). University of Alaska Fairbanks. https://doi.org/10.4027/mhmta.2008.04

Chadwick, J., Perfit, M., Ridley, I., Jonasson, I., Kamenov, G., Chadwick, W. W., et al. (2005). Magmatic effects of the Cobb hot spot on the Juan de Fuca Ridge. *Journal of Geophysical Research: Solid Earth*, *110*(B3), 110. https://doi.org/10.1029/2003jb002767

Chadwick, W. W. (2013). *Processed Gridded (ESRI ASCII format) Swath Bathymetry Data from the Juan de Fuca Axial Seamount acquired during the Thomas G. Thompson expedition TN253 (2010)*. Interdisciplinary Earth Data Alliance (IEDA). https://doi.org/10.1594/IEDA/316779

Chadwick, W. W., Clague, D. A., Embley, R. W., Perfit, M. R., Butterfield, D. A., Caress, D. W., et al. (2013). The 1998 eruption of Axial Seamount: New insights on submarine lava flow emplacement from high-resolution mapping. *Geochemistry, Geophysics, Geosystems*, *14*(10), 3939–3968. https://doi.org/10.1002/ggge.20202

Chadwick, W. W., & Embley, R. W. (1998). Graben formation associated with recent dike intrusions and volcanic eruptions on the mid-ocean ridge. *Journal of Geophysical Research: Solid Earth*, *103*(B5), 9807–9825. https://doi.org/10.1029/97JB02485

Chadwick, W. W., Jr., Paduan, J. B., Clague, D. A., Dreyer, B. M., Merle, S. G., Bobbitt, A. M., et al. (2016). Voluminous eruption from a zoned magma body after an increase in supply rate at Axial Seamount. *Geophysical Research Letters*, *43*(23), 12063–12070. https://doi.org/10.1002/2016GL071327

Clague, D. A., Paduan, J., Caress, D., Chadwick, W., Le Saout, M., Dreyer, B., & Portner, R. (2017). High-resolution AUV mapping and targeted ROV observations of three historical lava flows at Axial Seamount. *Oceanography*, *30*(4). https://doi.org/10.5670/oceanog.2017.426

Clague, D. A., Portner, R. A., Paduan, J. B., Le Saout, M., & Dreyer, B. M. (2019). Formation of the summit caldera at Axial Seamount. In *Presented at the AGU 2019 Fall Meeting; 9–13 December 2019, San Francisco*. Retrieved from https://ui.adsabs.harvard.edu/abs/2019AGUFM.V43C0217C/abstract

Cowie, P. A. (1998). Normal fault growth in three-dimensions in continental and oceanic crust. In W. R. Buck, P. T. Delaney, J. A. Karson, & Y. Lagabrielle (Eds.), *Faulting and magmatism at mid-ocean ridges*. *Geophysical Monograph Series* (Vol. 106, pp. 325–348). American Geophysical Union. https://doi.org/10.1029/GM106p0325

Cowie, P. A., Scholz, C. H., Edwards, M., & Malinverno, A. (1993). Fault strain and seismic coupling on mid-ocean ridges. *Journal of Geophysical Research: Solid Earth*, *98*(B10), 17911–17920. https://doi.org/10.1029/93JB01567

DeMets, C., Gordon, R. G., & Argus, D. F. (2010). Geologically current plate motions. *Geophysical Journal International*, *181*(1), 1–80. https://doi.org/10.1111/j.1365-246x.2009.04491.x

Deschamps, A., Tivey, M., Embley, R. W., & Chadwick, W. W. (2007). Quantitative study of the deformation at Southern Explorer Ridge using high-resolution bathymetric data. *Earth and Planetary Science Letters*, *259*(1–2), 1–17. https://doi.org/10.1016/j.epsl.2007.04.007

Detrick, R., Sinton, J., Ito, G., Canales, J., Behn, M., Blacic, T., et al. (2002). Correlated geophysical, geochemical, and volcanological manifestations of plume-ridge interaction along the Galápagos Spreading Center. *Geochemistry, Geophysics, Geosystems*, *3*(10), 1–14. https://doi.org/10.1029/2002GC000350

Dziak, R. P., & Fox, C. G. (1999). The January 1998 earthquake swarm at Axial Volcano, Juan de Fuca Ridge: Hydroacoustic evidence of seafloor volcanic activity. *Geophysical Research Letters*, *26*(23), 3429–3432. https://doi.org/10.1029/1999GL002332

Escartín, J., Cowie, P. A., Searle, R., Allerton, S., Mitchell, N., MacLeod, C. J., & Slootweg, A. (1999). Quantifying tectonic strain and magmatic accretion at a slow spreading ridge segment, Mid-Atlantic Ridge, 29°N. *Journal of Geophysical Research: Solid Earth*, *104*(B5), 10421–10437. https://doi.org/10.1029/1998JB900097

Escartín, J., Soule, S. A., Fornari, D., Tivey, M., Schouten, H., & Perfit, M. R. (2007). Interplay between faults and lava flows in construction of the upper oceanic crust: The East Pacific Rise crest 9°25′–9°58′N. *Geochemistry, Geophysics, Geosystems*, *8*(6). https://doi.org/10.1029/2006GC001399

Head, J. W., Wilson, L., & Smith, D. K. (1996). Mid-ocean ridge eruptive vent morphology and substructure: Evidence for dike widths, eruption rates, and evolution of eruptions and axial volcanic ridges. *Journal of Geophysical Research: Solid Earth*, *101*(B12), 28265–28280. https://doi.org/10.1029/96JB02275

Howell, S. M., Ito, G., Behn, M. D., Martinez, F., Olive, J.-A., & Escartín, J. (2016). Magmatic and tectonic extension at the Chile Ridge: Evidence for mantle controls on ridge segmentation. *Geochemistry, Geophysics, Geosystems*, *17*, 2354–2373. https://doi.org/10.1002/2016GC006380

Ito, G., & Behn, M. D. (2008). Magmatic and tectonic extension at mid-ocean ridges: 2. Origin of axial morphology. *Geochemistry, Geophysics, Geosystems*, *9*(9). https://doi.org/10.1029/2008GC001970

Kent, G. M., Singh, S. C., Harding, A. J., Sinha, M. C., Orcutt, J. A., Barton, P. J., et al. (2000). Evidence from three-dimensional seismic reflectivity images for enhanced melt supply beneath mid-ocean-ridge discontinuities. *Nature*, *406*, 614–618. https://doi.org/10.1038/35020543

Lee, M., & Carbotte, S. M. (2019). Detection of magma beneath the northern and southern rifts zones of Axial Seamount. In *Presented at the AGU 2019 Fall Meeting: 9–13 December 2019, San Francisco*. Retrieved from https://ui.adsabs.harvard.edu/abs/2019AGUFMOS51B1485L/abstract

Le Saout, M., Clague, D. A., & Paduan, J. B. (2019). Evolution of fine-scale segmentation at intermediate-spreading rate ridges. *Geochemistry, Geophysics, Geosystems*, *20*(8), 3841–3860. https://doi.org/10.1029/2019gc008218

Le Saout, M., Thibaud, R., & Gente, P. (2018). Detailed analysis of near tectonic features along the East Pacific Rise at 16°N, near the Mathematician Hot Spot. *Journal of Geophysical Research: Solid Earth*, *123*(6), 4478–4499. https://doi.org/10.1029/2017jb015301

Macdonald, K. C., & Fox, P. J. (1983). Overlapping spreading centres: New accretion geometry on the East Pacific Rise. *Nature*, *302*(5903), 55–58. https://doi.org/10.1038/302055a0

Macdonald, K. C., Fox, P. J., Miller, S., Carbotte, S., Edwards, M. H., Eisen, M. F., et al. (1992). The East Pacific Rise and its flanks 8°18′N: History of segmentation, propagation and spreading direction based on SeaMARC II and Sea Beam studies. *Marine Geophysical Researches*, *14*(4), 299–344. https://doi.org/10.1007/BF01203621

Macdonald, K. C., Fox, P. J., Perram, L. J., Eisen, M. F., Haymon, R. M., Miller, S. P., et al. (1988). A new view of the mid-ocean ridge from the behaviour of ridge-axis discontinuities. *Nature*, *335*, 217–225. https://doi.org/10.1038/335217a0

MacLeod, C. J., Searle, R. C., Murton, B. J., Casey, J. F., Mallows, C., Unsworth, S. C., et al. (2009). Life cycle of oceanic core complexes. *Earth and Planetary Science Letters*, *287*(3–4), 333–344. https://doi.org/10.1016/j.epsl.2009.08.016

Mastin, L. G., & Pollard, D. D. (1988). Surface deformation and shallow dike intrusion processes at Inyo Craters, long Valley, California. *Journal of Geophysical Research*, *93*(B11), 13221–13235. https://doi.org/10.1029/JB093iB11p13221

Neumann, G. A., & Forsyth, D. W. (1993). The paradox of the axial profile: Isostatic compensation along the axis of the Mid-Atlantic Ridge? *Journal of Geophysical Research: Solid Earth*, *98*(B10), 17891–17910. https://doi.org/10.1029/93jb01550

Olive, J.-A., & Dublanchet, P. (2020). Controls on the magmatic fraction of extension at mid-ocean ridges. *Earth and Planetary Science Letters*, *549*, 116541. https://doi.org/10.1016/j.epsl.2020.116541

Olive, J.-A., & Escartín, J. (2016). Dependence of seismic coupling on normal fault style along the Northern Mid-Atlantic Ridge. *Geochemistry, Geophysics, Geosystems*, *17*(10), 4128–4152. https://doi.org/10.1002/2016gc006460

Paduan, J. B., Clague, D. A., Caress, D. W., Le Saout, M., & Dreyer, B. M. (2020). Systematic variations in lava flow morphology along the north and south rift zones of Axial Seamount. In *Presented at the AGU 2020 Fall Meeting; 01–17 December 2020, virtual*. Retrieved from https://www.essoar.org/doi/abs/10.1002/essoar.10505810.1

Phipps Morgan, J., & Chen, Y. J. (1993). Dependence of ridge-axis morphology on magma supply and spreading rate. *Nature*, *364*(6439), 706–708. https://doi.org/10.1038/364706a0

Pollard, D. D., Delaney, P. T., Duffield, W. A., Endo, E. T., & Okamura, A. T. (1983). Surface deformation in volcanic rift zones. *Tectonophysics*, *94*(1–4), 541–584. https://doi.org/10.1016/0040-1951(83)90034-3

Qin, R., & Buck, R. W. (2008). Why meter-wide dikes at oceanic spreading centers? *Earth and Planetary Science Letters*, *265*(3–4), 466–474. https://doi.org/10.1016/j.epsl.2007.10.044

Ramsey, J. M., & Chester, F. M. (2004). Hybrid fracture and the transition from extension fracture to shear fracture. *Nature*, *428*, 63–66. https://doi.org/10.1038/nature02333

Rubin, A. M. (1992). Dike-induced faulting and graben subsidence in volcanic rift zones. *Journal of Geophysical Research: Solid Earth*, *97*(B2), 1839–1858. https://doi.org/10.1029/91JB02170

Schouten, H., Klitgord, K. D., & Whitehead, J. A. (1985). Segmentation of mid-ocean ridges. *Nature*, *317*(6034), 225–229. https://doi.org/10.1038/317225a0

Schouten, H., Smith, D. K., Cann, J. R., & Escartín, J. (2010). Tectonic versus magmatic extension in the presence of core complexes at slow-spreading ridges from a visualization of faulted seafloor topography. *Geology*, *38*(7), 615–618. https://doi.org/10.1130/g30803.1

Shah, A., & Buck, W. R. (2003). Plate bending stresses at axial highs, and implications for faulting behavior. *Earth and Planetary Science Letters*, *211*, 343–356. https://doi.org/10.1016/S0012-821X(03)00187-0

Shaw, W. J., & Lin, J. (1996). Models of ocean ridge lithospheric deformation: Dependence on crustal thickness, spreading rate, and segmentation. *Journal of Geophysical Research: Solid Earth*, *101*(B8), 17977–17993. https://doi.org/10.1029/96JB00949

Sinton, J., Bergmanis, E., Rubin, K., Batiza, R., Gregg, T. K., Grönvold, K., et al. (2002). Volcanic eruptions on mid-ocean ridges: New evidence from the superfast spreading East Pacific Rise, 17°–19°S. *Journal of Geophysical Research: Solid Earth*, *107*(B6). ECV 3-1–ECV 3-20. https://doi.org/10.1029/2000JB000090

Sleep, N. H. (1975). Formation of oceanic crust: Some thermal constraints. *Journal of Geophysical Research*, *80*(29), 4037–4042. https://doi.org/10.1029/JB080i029p04037

VanderBeek, B. P., Toomey, D. R., Hooft, E. E. E., & Wilcock, W. S. D. (2016). Segmentation of mid-ocean ridges attributed to oblique mantle divergence. *Nature Geoscience*, *9*, 636–642. https://doi.org/10.1038/ngeo2745

White, S. M., Mason, J. L., Macdonald, K. C., Perfit, M. R., Wanless, V. D., & Klein, E. M. (2009). Significance of widespread low effusion rate eruptions over the past two million years for delivery of magma to the overlapping spreading centers at 9°N East Pacific Rise. *Earth and Planetary Science Letters*, *280*(1–4), 175–184. https://doi.org/10.1016/j.epsl.2009.01.030

Wilson, D. S. (1993). Confidence intervals for motion and deformation of the Juan de Fuca Plate. *Journal of Geophysical Research: Solid Earth*, *98*(B9), 16053–16071. https://doi.org/10.1029/93jb01227